COMPONENT PART NOTICE

THIS PAPER IS A COMPONENT PART OF THE FOLLOWING COMPILATION REPORT:

TITLE: Theoretical Aspects of Target Classification. Lecture Series on Electromagnetic Wave Propagation Panel and the Consultant and Exchange Programme Held in Rome, Italy on 29-30 June 1987; Neubiberg, Germany on 2-3 July 1987 and Noresund, Norway on 6-7 July 1987.

TO ORDER THE COMPLETE COMPILATION REPORT, USE AD-A185 125.

THE COMPONENT PART IS PROVIDED HERE TO ALLOW USERS ACCESS TO INDIVIDUALLY AUTHORED SECTIONS OF PROCEEDING, ANNALS, SYMPOSIA, ETC. HOWEVER, THE COMPONENT SHOULD BE CONSIDERED WITHIN THE CONTEXT OF THE OVERALL COMPILATION REPORT AND NOT AS A STAND-ALONE TECHNICAL REPORT.

THE FOLLOWING COMPONENT PART NUMBERS COMPRISE THE COMPILATION REPORT:

AD#: P005 644 through	AD#: P005 655
AD#:	AD#:
AD#:	AD#:

Accession For	
NTIS GRA&I	X
DTIC TAB	☐
Unannounced	☐
Justification	
By	
Distribution/	
Availability Codes	
Dist	Avail and/or Special
A-1	

DTIC ELECTE OCT 2 6 1987 S D E

This document has been approved for public release and sale; its distribution is unlimited.

DTIC FORM MAR 85 463

OPI: DTIC-TID

UNIFORM GEOMETRICAL THEORY OF DIFFRACTION

by
P.H. Pathak
The Ohio State University ElectroScience Laboratory
1320 Kinnear Road
Columbus, Ohio 43212

SUMMARY

Keller's geometrical theory of diffraction (GTD) represents a major breakthrough in solving a wide variety of electromagnetic (EM) radiation and scattering problems at high frequencies. In particular, the GTD is an extension of geometrical optics to include a class of diffracted rays via a generalization of Fermat's principle. These diffracted rays are initiated, for example, from geometrical and electrical discontinuities in a scatterer, or from points of grazing incidence on smooth convex parts of the scattering surface. However, being a purely ray optical theory, the original GTD fails within the transition regions adjacent to geometric optical shadow boundaries where the diffracted field generally assumes its largest value. This limitation of the GTD is overcome via the uniform version of the GTD (i.e., UTD) which requires the diffracted field to make the total high frequency field continuous across the optical shadow boundaries. The UTD solutions for the diffraction by edges and smooth convex surfaces are reviewed in detail after introducing the basic concepts of GTD. Results based on a few additional UTD solutions are also presented together with a few selected applications of these UTD solutions to predict the EM radiation and scattering from complex structures.

I. INTRODUCTION

An efficient analysis of the radiation and scattering of waves by objects which are large in terms of the wavelength can be performed via high frequency techniques. One of the most versatile and useful high frequency (HF) techniques is Keller's geometrical theory of diffraction (GTD) [1,2,3] which was developed in the early 1950s. The GTD constitutes a significant extension of geometrical optics (GO) in which a class of diffracted rays are introduced to exist in addition to the usual rays of GO. These diffracted rays are postulated via a generalization of Fermat's principle with the knowledge that at high frequencies diffraction, like reflection, is a highly local phenomenon. Just as reflected rays originate from points of specular reflection on an illuminated surface, the diffracted rays likewise originate from certain localized parts on the surface; e.g., from geometrical and electrical discontinuities, and from points of grazing incidence on a smooth convex surface as shown in Figure 1.

The shadow boundaries divide the space surrounding an illuminated body into a lit region where the GO incident, reflected and refracted rays are present, and into a shadow region where these GO rays are absent. Thus, the GO approach is seriously in error within the shadow region where it predicts a zero field; this limitation of GO is overcome by the GTD since the diffracted rays penetrate into the GO shadow zone to entirely account for the field therein. Furthermore, the diffracted rays can also enter into the lit region and thereby provide an improvement to GO in the lit region. The total GTD field is a superposition of the field of all the GO incident, reflected and refracted rays together with the field of all the diffracted rays which pass through the observation point. The initial values of the diffracted ray fields are given in terms of the diffraction coefficients just as the initial amplitudes of the GO reflected and refracted rays are given in terms of the reflection and transmission coefficients.

Due to the local nature of diffraction at high frequencies, the diffraction coefficients can be found from the appropriate solutions to simpler canonical problems which model the geometrical and electrical properties in the neighborhood of the point of diffraction as in the original problem. Consequently, the GTD provides an efficient high frequency solution to problems that cannot be solved rigorously. Thus, a GTD analysis of the radiation/scattering from complex shapes can be developed by simulating these structures with simpler shapes that locally provide a sufficiently accurate description of the dominant reflection and diffraction effects. The GTD can also be useful in providing information on ways to control the radiation/scattering from different parts of the structure. It is interesting that even though GTD is a high frequency method, it is often found to work for objects nearly as small as a wavelength in size. Although GTD is not a rigorous method, it generally yields the leading terms in the asymptotic high frequency solutions of diffraction problems.

Since the GTD is a purely ray optical theory, it fails within the transition regions adjacent to the GO shadow boundaries where the HF field generally undergoes a rapid transition across the shadow boundary from one ray optical form in the lit region to another ray optical form in the shadow region. Consequently, the HF field departs from a strictly ray optical character within the GO shadow boundary transition regions. This failure of the original GTD can be overcome by uniform versions of the GTD such as the UTD [4,5] and the UAT [6]. In the present development, the focus will be on the UTD. Basically, the UTD remains valid within the GO shadow boundary transition regions where the ordinary GTD fails, and secondly, it reduces to the GTD outside these transition regions where the latter is indeed valid.

The GTD and its uniform versions (UTD;UAT) fail within the regions of GO and diffracted ray caustics. Ray caustics or focii occur whenever a family of rays (i.e., ray congruences) merge or intersect to form a focal surface, or a focal line or a focal point. The field near diffracted ray caustics can be described with the help of the equivalent current method (ECM) [7,8,9] in which the GTD indirectly provides the strengths of these equivalent currents that radiate fields at and near the caustics. Away from the caustics, the ECM usually reduces to the GTD. The ECM can in general be used provided the GO shadow boundaries and caustics do not overlap. In the latter situation, ECM could in some cases still be used but only after significant modification; alternatively, the physical theory of diffraction (PTD) can be employed. The PTD was introduced by Ufimtsev [10] in the Soviet Union at about the same time as Keller's GTD was introduced in the U.S. The PTD requires an integration of the asymptotic HF currents on the radiating/scattering body. If the PTD integrals can be evaluated asymptotically outside the confluence of GO shadow boundary and caustic regions, then it generally reduces to the GTD. However, in some special instances, the GTD can be made to work without resorting to ECM or PTD despite a presence of a confluence of caustic and GO shadow boundary transition regions. Away from the special regions where it may be necessary to use ECM or PTD, it is natural to employ the more efficient GTD/UTD which unlike the ECM and PTD requires no integration [11].

These notes will deal mostly with the diffraction by perfectly-conducting surfaces in free space. The GTD formulation is presented after briefly introducing the concept of wavefronts, rays and GO in Section II. Next, the UTD is discussed and UTD expressions are given for the two main diffraction mechanisms; namely, for edge diffraction and diffraction at a smooth convex surface. Other UTD solutions are not included due to space limitations. Finally, a few examples illsutrating the utility of UTD to analyze radiation and scattering problems are given in Section III. An $e^{j\omega t}$ time dependence is assumed and suppressed in the following development.

II. THE GTD AND ITS UNIFORM VERSION -- THE UTD

The basic ideas of wavefronts, rays and GO are briefly reviewed at first. Diffracted rays which exist in addition to the GO rays are discussed subsequently.

A. Wavefronts and Rays

A wavefront is an equiphase surface. The connection between wavefronts and rays can be made in several ways. One such procedure which is based on the method of stationary phase is described below. Let $\bar{E}(\bar{r}')$ and $\bar{H}(\bar{r}')$ refer to the electric and magnetic field intensities at any point $\bar{r}'$ on an equiphase (or wavefront) surface S. The electric field $\bar{E}(\bar{r})$ at a point P ahead of the wavefront is provided by the equivalence theorem as:

$$\bar{E}(\bar{r}) = \iint_S ds' \left(\frac{jkZ_0}{4\pi}\right)[\hat{R} \times \hat{R} \times \bar{J}_s(\bar{r}') + Y_0\hat{R} \times \bar{M}_s(\bar{r}')] \frac{e^{-jkR}}{R} \tag{1}$$

in which the equivalent electric and magnetic surface current sources $\bar{J}_s$ and $\bar{M}_s$, respectively on S are

$$\bar{J}_s(\bar{r}') = \hat{n}' \times \bar{H}(\bar{r}') \ ; \ \bar{M}_s(\bar{r}') = \bar{E}(\bar{r}') \times \hat{n}' \ . \tag{2a,2b}$$

The quantity Z_0 denotes the impedance of free space, and $Y_0=(Z_0)^{-1}$. Also, k represents the wave number of free space. The vector $\bar{R}$ and the unit normal vector $\hat{n}'$ to the surface S at $\bar{r}'$ are shown in Figure 2.

Consider a rectangular coordinate system chosen for convenience so that the x and y axes are tangent to the wavefront at O, and $\overline{OP} = \hat{z}|\overline{OP}|$ as in Figure 2. It is noted that $\hat{n}'=\hat{z}$ at O. It is generally true that there is at least one point O on S so that $\overline{OP} = \hat{n}'|\overline{OP}|$; however, for the present development it is assumed that there is only one such point O. If there are more points on S with the above property such that the $\hat{n}'$ directions from those points intersect at P, then P is said to be a focal or caustic point. From the principle of stationary phase as described for example by Silver [12], the e^{-jkR} within the integrand of (1) oscillates rapidly for large k to produce a cancellation (destructive interference) between each of the spherical wave contributions to P which arise from the different elemental sources on ds' over S that do not lie in the immediate neighborhood of O; whereas, e^{-jkR} changes slowly for the spherical wave contributions to P arising from the elemental sources on ds' that are in the immediate neighborhood of O and thereby provide a constructive interference to P. Thus, at high frequencies (or large k), the dominant field contribution to P comes from O on S; this point O is called the "stationary point." Without details (which can be found in [12]), the stationary phase evaluation of (1) yields the following contribution from the stationary point:

$$\bar{E}(P) \sim \bar{E}(O)\sqrt{\frac{\rho_1}{(\rho_1+s)} \frac{\rho_2}{(\rho_2+s)}} \ e^{-jks} \ ; \ |\overline{OP}|=s \ . \tag{3}$$

The expression in (3) describes the continuation of the field at O to the field at P along the highly localized or "ray" path $\overline{OP}$; the field $\bar{E}(P)$ in (3) is thus referred to as a ray optical field. Figure 3 shows a ray tube interpretation of the energy transport along the central ray $\overline{OP}$ as indicated by (3). The ρ_1 and ρ_2 in (3) refer to the principal wavefront radii of curvatures at O. From Figure 3 one notes that the energy flux crossing the area dA_0 of the wavefront at O is given by $|\bar{E}(O)|^2 \ dA_0$, and likewise, the energy flux crossing the area dA_p of the same ray tube is $|\bar{E}(P)|^2dA_p$. Since $dA_0=(\rho_1d\psi_1)(\rho_2d\psi_2)$ and $dA_p=[(\rho_1+s)d\psi_1][(\rho_2+s)d\psi_2]$, it is then clear that conservation of energy in a ray tube, which in turn requires that $|\bar{E}(O)|^2dA_0=|\bar{E}(P)|^2dA_p$, leads to

$$|\bar{E}(P)|^2 = |\bar{E}(O)|^2 \left| \frac{\rho_1 \ \rho_2}{(\rho_1+s)(\rho_2+s)} \right| \ , \tag{4}$$

which is automatically implied in (3). The field $\bar{E}(P)$ at P has the same polarization as the field $\bar{E}(O)$ at O because the ray path is straight in a homogeneous medium. The field intensity in (3) becomes singular when $s=-|\rho_1|$ or $s=-|\rho_2|$; these points on the ray path are marked (3-4) and (1-2) in Figure 3, and they are referred to as ray caustics. The actual field is not singular at the caustics; clearly the simple expression in (3) is therefore not valid at and near the caustic, even though it is asymptotically accurate away from the caustics. The distances ρ_1 and ρ_2 are also referred to as caustic distances. The distance s is measured positive in the direction of ray propagation. The caustic distances ρ_1 and ρ_2 are positive if the caustics occur before the reference point O as one propagates along the ray; otherwise, they are negative. If ρ_1 and ρ_2 are positive, the wavefront is convex; if they are negative, the wavefront is concave. If one of the radii (ρ_1 or ρ_2) is positive while the other is negative then the wavefront is saddleshaped. If ρ_1 and ρ_2 are negative, and if $s>-|\rho_1|$, or $s>-|\rho_2|$, then a caustic is crossed at (3-4) or (1-2) in Figure 3, respectively so that $((\rho_1)/(\rho_1+s))$ or $((\rho_2)/(\rho_2+s))$ changes sign within the square root of (3). The positive branch of the square root is chosen in (3) so that

$$\sqrt{\frac{\rho}{\rho+s}} = \left|\sqrt{\frac{\rho}{\rho+s}}\right| e^{j\left\{{0 \atop \pi/2}\right\}} \quad , \text{ if } \left(\frac{\rho}{\rho+s}\right) \gtrless 0 \quad , \tag{5}$$

and $\rho = \rho_1$ or ρ_2. Thus, a phase jump of $\pi/2$ occurs at each causting crossing.

The field in (3) is sometimes also referred to as an "arbitrary" ray optical field since ρ_1 and ρ_2 can be "arbitrary." The geometry in Figure 3 is referred to as an astigmatic ray tube or a quadratic ray pencil because of the quadratic wavefront surface approximation at O that is used in the stationary phase approach leading to (3). It is noted that if ρ_1 and ρ_2 become infinite, then the field in (3) is that of a plane wave. If ρ_1 or ρ_2 become infinite then (3) is a cylindrical wave field. Also, if $\rho_1 = \rho_2$ (=finite value), then (3) is a spherical wave field. Thus, plane, cylindrical, spherical and even conical wave fields are special cases of an arbitrary ray optical field; clearly, it follows that each of these fields is also ray optical.

Since the wavefront surface S in Figure 3 can be associated with either an incident, reflected or diffracted wave, the field expression in (3) therefore applies equally to incident, reflected or diffracted rays. The field is polarized transverse to the ray and the wavefront at P is "locally" plane if ks is sufficiently large (as is assumed to be true in the stationary phase evaluation leading to (3)); also, the local plane wave relation between $\bar{E}$ and $\bar{H}$ holds, namely:

$$\bar{H}(P) \approx Y_0 \, \hat{s} \times \bar{E}(P) \tag{6}$$

or

$$\bar{E}(P) \approx - Z_0 \hat{s} \times \bar{H}(P) \tag{7}$$

in which $\hat{s} = \overline{OP}/|\overline{OP}|$ is the ray direction.

B. The GO Field

The GO field is a ray optical field. The incident GO field is associated with rays directly radiated from the source to the field point. When such an incident ray congruence strikes an object, it is transformed into a reflected ray congruence. Since the present notes deal mostly with scattering by impenetrable objects, there are no transmitted or refracted rays produced in this case. The incident and reflected GO rays satisfy Fermat's principle which makes the incident and reflected ray paths an extremal. Consider a plane wave incident on a perfectly-conducting wedge or a smooth convex surface as shown in Figures 4(a) or 4(b). The incident rays are partly blocked by these surfaces creating the so-called shadow zone where the incident ray optical field vanishes. The incident shadow boundary ISB in Figure 4(a) and the surface shadow boundary SSB in Figure 4(b) divide the region of space surrounding the wedge and the convex surface into a lit zone and a shadow zone.

It is important to note that unlike the conventional incident field which is defined to exist in the absence of any scattering objects, the GO incident ray field exists in the presence of any objects that it might illuminate. It is for this reason that the GO incident field becomes discontinuous across the shadow boundaries ISB and SSB in Figures 4(a) and 4(b). On the other hand, the conventional incident field would not be discontinuous anywhere outside the source region which produced that field. Henceforth, the GO incident electric and magnetic fields will be denoted by $\bar{E}^i$ and $\bar{H}^i$, respectivel

The field of the GO reflected rays that are produced by the illuminated wedge in Figure 4(a) is also discontinuous. In particular, the reflection shadow boundary (RSB) delineates the regions of existence and shadow for the reflected rays in Figure 4(a); whereas, the incident and reflection shadow boundaries ISB and RSB merge into the SSB for the convex surface in Figure 4(b).

Consider a general problem of reflection where an arbitrary GO incident ray optical field illuminates a smooth, perfectly-conducting curved surface. The astigmatic incident ray tube associated with the incident ray in the direction $\hat{s}^i$ is shown in Figure 5. This incident ray strikes the surface at O_R to produce a reflected ray in the direction $\hat{s}^r$. The astigmatic reflected ray tube associated with the reflected ray from O_R is also shown in Figure 5. The field $\bar{E}^r(P)$ at P which is reflected from O_R can be written via (3) as:

$$\bar{E}^r(P) = \bar{E}^r(O_R) \sqrt{\frac{\rho_1^r}{(\rho_1^r + s^r)} \, \frac{\rho_2^r}{(\rho_2^r + s^r)}} \; e^{-jks^r} \quad . \tag{8}$$

It is noted that $\bar{E}^r(P)$ in (8) is given in terms of $\bar{E}^r(O_R)$ at the point of reflection O_R. Thus, the reference point O in (3) corresponds to the point O_R in (8). The caustic distances ρ_1^r and ρ_2^r associated with the reflected wavefront are shown in Figure 5 along with the reflected ray distance s^r from O_R to P. The value of $\bar{E}^r(O_R)$ is related to the incident field $\bar{E}^i(O_R)$ via the boundary condition

$$\hat{n} \times (\bar{E}^i(Q_R) + \bar{E}^r(Q_R)) = 0 \quad . \tag{9}$$

Here, $\hat{n}$ is the unit normal vector to the surface at Q_R. It follows from (9) that

$$\bar{E}^r(Q_R) = \bar{\bar{R}} \cdot \bar{E}^i(Q_R) \quad , \tag{10}$$

where $\bar{\bar{R}}$ is the dyadic reflection coefficient of the surface at Q_R. Incorporating (9) into (8) yields

$$\bar{E}^r(P) = \bar{E}^i(Q_R) \cdot \bar{\bar{R}} \sqrt{\frac{\rho_1^r}{\rho_1^r+s^r} \cdot \frac{\rho_2^r}{\rho_2^r+s^r}}\ e^{-jks^r} \quad . \tag{11}$$

The reflected magnetic field $\bar{H}^r(P)$ is found easily from (11) via

$$\bar{H}^r(P) \sim Y_o \hat{s}^r \times \bar{E}^r(P) \quad . \tag{12}$$

It is convenient to express $\bar{E}^i(Q_R)$ and $\bar{E}^r(P)$ in terms of the unit vectors $(\hat{e}_\parallel^i, \hat{e}_\perp)$ and $(\hat{e}_\parallel^r, \hat{e}_\perp)$ which are fixed in the incident and reflected rays, respectively, as shown in Figure 6. The $\hat{e}_\parallel^i, \hat{e}_\perp$ and $\hat{s}^i$ are mutually orthogonal; likewise, $\hat{e}_\parallel^r, \hat{e}_\perp$ and $\hat{s}^r$ are also a mutually orthogonal set. Furthermore, $\hat{e}_\parallel^i$ and $\hat{e}_\parallel^r$ lie in the plane of incidence defined by $\hat{s}^i$ and $\hat{n}$ at Q_R. As a result of Fermat's principle, $\hat{s}^r$ also lies in the plane of incidence and $\theta^i = \theta^r$ in Figure 6. Thus, if

$$\bar{E}^i(Q_R) = E_\parallel^i(Q_R)\, \hat{e}_\parallel^i + E_\perp^i(Q_R)\, \hat{e}_\perp \tag{13}$$

and

$$\bar{E}^r(P) = E_\parallel^r(P)\hat{e}_\parallel^r + E_\perp^r(P)\hat{e}_\perp \tag{14}$$

where $\hat{e}_\perp = \hat{s}^{i,r} \times \hat{e}_\parallel^{i,r}$, then $\bar{\bar{R}}$ in (10) subject to the boundary condition (9) becomes

$$\bar{\bar{R}} = \hat{e}_\parallel^i\, \hat{e}_\parallel^r\, R_h + \hat{e}_\perp\, \hat{e}_\perp\, R_s \quad ; R_{\substack{s\\h}} = \mp 1 \ . \tag{15}$$

In matrix notation, the above $\bar{\bar{R}}$ can be written as

$$\begin{bmatrix} R_h & 0 \\ 0 & R_s \end{bmatrix} = \begin{bmatrix} 1 & 0 \\ 0 & -1 \end{bmatrix} . \tag{16}$$

Therefore, in matrix notation, (11) becomes

$$\begin{bmatrix} E_\parallel^r(P) \\ E_\perp^r(P) \end{bmatrix} = \begin{bmatrix} 1 & 0 \\ 0 & -1 \end{bmatrix} \begin{bmatrix} E_\parallel^i(Q_R) \\ E_\perp^i(Q_R) \end{bmatrix} \sqrt{\frac{\rho_1^r\, \rho_2^r}{(\rho_1^r+s^r)(\rho_2^r+s^r)}}\ e^{-jks^r} \ , \tag{17}$$

The caustic distances or the principal radii of curvature of the incident and reflected wavefronts which are denoted by (ρ_1^i, ρ_2^i) and (ρ_1^r, ρ_2^r), as well as their principal wavefront directions are given in [13].

It is clear that the GO representation of (11) fails at caustics which are the intersection of the paraxial rays (associated with the ray tube or pencil) at the lines 1-2 and 3-4 as shown in Figure 3. Upon crossing a caustic in the direction of propagation, $(\rho^{i,r}+s^{i,r})$ changes sign under the radical in and a phase jump of $+\pi/2$ results as explained earlier. Furthermore, the reflected field $\bar{E}^r$ of (11) fails in the transition region adjacent to SSB of Figure 4(b). It is important to note that near the SSB (i.e., as $\theta^i \to \pi/2$), ρ_1^r and ρ_2^r approach the following limiting values:

$$\rho_2^r \to \frac{\rho_g(Q_R)\cos\theta^i}{2} \to 0 \qquad \text{for } \theta^i \to \pi/2 \tag{18a}$$

$$\rho_1^r \to \rho_b^i \; , \tag{18b}$$

where $\rho_g(Q_R)$ is the surface radius of curvature in the plane of incidence at Q_R, and ρ_b^i is the radius of curvature of the incident wavefront in the $(\hat{t},\hat{b})$ plane (i.e., in the plane tangent to the surface) at Q_R for $\theta^i \to \pi/2$. Furthermore, the principal directions $\hat{X}_1^r$ and $\hat{X}_2^r$ of the reflected wavefront approach the following values for grazing incidence:

$$\hat{X}_1^r \to \hat{b} \quad (\text{at } Q_R) \tag{19}$$

$$\text{for } \theta^i \to \pi/2 \quad ,$$

$$\hat{X}_2^r = (-\hat{s}^r \times \hat{X}_1^r) \to \hat{n} \quad (\text{at } Q_R) \tag{20}$$

where $\hat{t}$ is the direction of grazing incidence at Q_R and $\hat{b}=\hat{t} \times \hat{n}$ at Q_R. The total GO electric field E^{GO} at P_L in the lit region is the sum of the incident and reflected ray optical fields; hence,

$$\bar{E}^{GO}(P_L) \sim \bar{E}^i(P_L) + \bar{E}^i(Q_R)\cdot \bar{R}\sqrt{\frac{\rho_1^r \rho_2^r}{(\rho_1^r+s^r)(\rho_2^r+s^r)}}\, e^{-jks^r} . \tag{21}$$

In summary, it is noted that the GO incident and reflected fields are discontinuous across their associated shadow boundaries such as ISB, RSB, and SSB in Figures 4(a) and 4(b). The failure of GO to account for a proper non-zero field within the shadow region behind an impenetrable obstacle can be overcome through the GTD and its uniform versions. Nevertheless, GO generally yields the dominant contribution to the total high frequency fields, and it constitutes the leading term in the GTD solution.

The reflected GO field $\bar{E}^r(P_L)$ for the two-dimensional (2-D) case can be deduced directly from the 3-D case by allowing ρ_1^r to approach infinity. Thus, one may let $\rho_2^r \equiv \rho^r$ and $\rho_1^r \to \infty$ in (11) to arrive at the 2-D reflected GO field $\bar{E}^r(P_L)$ as

$$\bar{E}^r(P_L) = \bar{E}^i(Q_R)\cdot \bar{\bar{R}}\sqrt{\frac{\rho^r}{\rho^r+s^r}}\; e^{-jks^r} \quad , \tag{22}$$

in which the incident ray optical field $\bar{E}^i(Q_R)$ is now a cylindrical wave at Q_R, and the caustic distance ρ^r in (22) for the 2-D case is given by

$$\frac{1}{\rho^r} = \frac{1}{s^i} + \frac{2\cos^{-1}\theta^i}{\rho_g(Q_R)} \quad , \tag{23}$$

where θ^i has the same meaning as before, and s^i is the radius of curvature of the incident cylindrical wavefront at Q_R. If the cylindrical wave is produced by a 2-D line source, then s^i in (22) can be chosen to be the distance from that line source to the point of reflection Q_R on the 2-D boundary. The quantity $\rho_g(Q_R)$ in (23) denotes the radius of curvature of the 2-D boundary at the point of reflection Q_R.

C. The Diffracted Ray Fields

The diffracted rays are introduced in the GTD via a generalization of Fermat's principle as stated previously. Away from the point of diffraction, the diffracted rays behave according to the laws of GO. The initial value of the diffracted ray field is given in terms of a diffraction coefficient. The phenomenon of edge diffraction will be discussed first, and it will be followed by a discussion on the phenomenon of diffraction at a smooth convex surface. The latter phenomenon is more complicated than the first.

(i) Edge Diffraction

When an incident ray strikes an edge in an otherwise smooth surface, it produces diffracted rays which lie on a cone about the tangent to the edge at the point of diffraction such that the angle β_0 between the incident ray and the edge tangent equals the half angle of the diffracted ray cone as shown in Figure 1(a). This cone of diffracted rays is sometimes referred to as the "Keller cone," and it results from the generalization of Fermat's principle to describe rays diffracted by an edge.

Let an arbitrary ray optical field be incident on a perfectly-conducting curved wedge as shown in Figure 7. The resultant total HF electric field $\bar{E}(P)$ at any point P exterior to the wedge is given by

$$\bar{E}(P) = \bar{E}^{GO}(P) + \bar{E}^{d}(P) \tag{24}$$

where the GO field component $\bar{E}^{GO}(P)$ is given as

$$\bar{E}^{GO}(P) = \bar{E}^{i}(P)U_i + \bar{E}^{r}(P)U_r \ . \tag{25}$$

The domains of existence of the incident and reflected ray optical fields $\bar{E}^{i}(P)$ and $\bar{E}^{r}(P)$ are indicated by the step functions U_i and U_r, respectively, which are defined as follows:

$$U_i = \begin{cases} 1, & \text{if } 0 < \phi < \pi+\phi' \\ 0, & \text{if } \pi+\phi' < \phi < n\pi \end{cases} \tag{26}$$

and

$$U_r = \begin{cases} 1, & \text{if } 0 < \phi < \pi-\phi' \\ 0, & \text{if } \pi-\phi' < \phi < n\pi \ . \end{cases} \tag{27}$$

The azimuthal angles ϕ and ϕ' are made by the projections of the directions of incidence and observation on a plane perpendicular to the edge at the point of diffraction Q_E. These angles are measured from a plane tangent to the "0" face of the wedge at Q_E as shown in Figure 8. The plane tangent to the other face of the wedge at Q_E is denoted by "$n\pi$;" it is also shown in Figure 8.

The interior wedge angle is therefore given by $(2-n)\pi$. The expressions for the GO incident and reflected fields have been discussed previously. The diffracted field $\bar{E}^{d}$ exists exterior to the wedge (i.e., for $0 < \phi < n\pi$). From (2), one may write the general field expression for theray diffracted in the direction $\hat{s}^{d}$ from Q_E as:

$$\bar{E}^{d}(P) \sim \bar{E}^{d}(P_o)\sqrt{\frac{\rho_1^d \rho_2^d}{(\rho_1^d + s_o^d)(\rho_2^d + s_o^d)}}\, e^{-jks_o^d} \ . \tag{28}$$

The diffracted ray tube corresponding to (28) is shown in Figure 7. The superscript "d" on $\rho^d_{1,2}$, and s^d_o denotes that these quantities are associated with the diffracted ray field component. In order to relate $\bar{E}^{d}(P)$ to the incident field at the point of edge diffraction Q_E, one moves the reference P_o in Figure 7 to the point of diffraction Q_E on the edge by letting $\rho_1^d \to 0$ so that

$$\bar{E}^{d}(P) = \lim_{\rho_1^d \to 0} \left[\sqrt{\rho_1^d}\, \bar{E}^{d}(P_o)\right] \sqrt{\frac{\rho_2^d}{(\rho_1^d + s_o^d)(\rho_2^d + s_o^d)}}\, e^{-jks_o^d} \ . \tag{29}$$

Since $\bar{E}^{d}(P)$ is independent of the reference point P_o, the above limit exists and it is defined as

$$\lim_{\rho_1^d \to 0} \sqrt{\rho_1^d}\, \bar{E}^{d}(P_o) \equiv \bar{E}^{i}(Q_E) \cdot \bar{\bar{D}}_e^k \ , \tag{30}$$

where $\bar{\bar{D}}_e^k = \bar{\bar{D}}_e^k(\phi,\phi',\beta_o;\, k)$ is Keller's "dyadic edge diffraction coefficient" which indicates how the energy is distributed in the diffracted field as a function of the angles ϕ, ϕ', and β_o; $\bar{\bar{D}}_e^k$ also depends on n and the wavenumber k. From (29) and (30), it is clear that

$$\bar{E}^{d}(P) \sim \bar{E}^{i}(Q_E) \cdot \bar{\bar{D}}_e^k(\phi,\phi',\beta_o;\, k)\sqrt{\frac{\rho_e}{s^d(\rho_e + s^d)}}\, e^{-jks^d} \ , \tag{31}$$

where $\lim_{\rho_1^d \to 0} \rho_2^d \equiv \rho_e$ (edge diffracted ray caustic distance), and likewise $\lim_{\rho_1^d \to 0} s_o^d \equiv s^d$, as shown in Figure 7. $\bar{E}^{d}(P)$ is polarized transverse to the diffracted ray direction $\hat{s}^{d}$ since the field $\bar{E}^{d}(P)$ is ray optical; thus, the associated magnetic field can be expressed as

$$\bar{H}^{d}(P) \sim Y_o\, \hat{s}^{d} \times \bar{E}^{d}(P) \ . \tag{32}$$

If the incident field $\bar{E}^i(Q_E)$ exhibits a rapid spatial variation at Q_E then an additional term referred to as a slope diffracted field must be included in (31) to describe the diffraction effects accurately; however, that slope diffracted field will not be described here. An expression for finding the diffracted ray caustic distance ρ_e is given later in (43b).

It is convenient to express the dyadic edge diffraction coefficient $\bar{\bar{D}}_e^k$ in terms of unit vectors fixed in the incident and diffracted rays as follows. Let $\hat{s}^i$ and $\hat{e}$ define an edge fixed plane of incidence where $\hat{e}$ is the edge tangent at Q_E. Likewise, let $\hat{s}^d$ and $\hat{e}$ define the edge fixed plane of diffraction. The law of edge diffraction which defines the Keller cone is $\hat{s}^i \cdot \hat{e} = \hat{s}^d \cdot \hat{e}$. Let $\hat{\beta}_0'$ and $\hat{\beta}_0$ be parallel to the edge fixed planes of incidence and diffraction, respectively as in Figure 8, and let

$$\hat{\beta}_0' = \hat{s}^i \times \hat{\phi}' \quad ; \quad \hat{\beta}_0 = \hat{s}^d \times \hat{\phi} . \tag{33a;33b}$$

Here, $\hat{\phi}$ and $\hat{\phi}'$ point in the direction of increasing angles ϕ and ϕ', respectively. The incident field $\bar{E}^i(Q_E)$ can then be expressed in terms of the triad of unit vectors $(\hat{s}^i, \hat{\beta}_0', \hat{\phi}')$ fixed in the incident ray; likewise, the edge diffracted field $\bar{E}^d(P)$ can be expressed in terms of $(\hat{s}^d, \hat{\beta}_0, \hat{\phi})$ fixed in the diffracted ray. Thus,

$$\bar{E}^i(Q_E) = \hat{\beta}_0' E^i_{\beta_0'} + \hat{\phi}' E^i_{\phi'} \tag{34a}$$

and

$$\bar{E}^d(P) = \hat{\beta}_0 E^d_{\beta_0} + \hat{\phi} E^d_{\phi} . \tag{34b}$$

Then

$$\bar{\bar{D}}_e^k = -\hat{\beta}_0' \hat{\beta}_0 D^k_{es} - \hat{\phi}' \hat{\phi} D^k_{eh} . \tag{34c}$$

The D^k_{es} and D^k_{eh} can be found from the asymptotic solutions of appropriate canonical wedge diffraction problems; they are given by:

$$D^k_{\substack{es\\eh}}(\phi,\phi';\beta_0) = \frac{e^{-j\frac{\pi}{4}} \sin\frac{\pi}{n}}{n\sqrt{2\pi k}\sin\beta_0} \cdot \left[\frac{1}{\cos\frac{\pi}{n} - \cos\left(\frac{\phi-\phi'}{n}\right)} \mp \frac{1}{\cos\frac{\pi}{n} - \cos\left(\frac{\phi+\phi'}{n}\right)} \right] . \tag{35}$$

It is noted that the Keller edge diffraction coefficient in (35) beomes singular at the incident shadow boundary (ISB) and the reflection shadow boundary (RSB) which occur when $\phi=\pi+\phi'$ and $\phi=\pi-\phi'$, respectively. Thus, the result in (31) together with (34c) and (35) is not valid at and near the GO incident and reflection shadow boundaries. This deficiency of the GTD can be overcome via the use of uniform geometrical theory of diffraction (UTD). According to the UTD [4,5], the total HF field exterior to the wedge is still given by (24) as in Keller's original GTD; however, the $\bar{E}^d$ in (24) and (31) is now modified so that $\bar{\bar{D}}_e^k$ of (31) is replaced by the UTD edge diffraction coefficient $\bar{\bar{D}}_e$ so that:

$$\bar{E}^d(P) = \bar{E}^i(Q_E) \cdot \bar{\bar{D}}_e(\phi, \phi', \beta_0; k) \sqrt{\frac{\rho_e}{s^d(\rho_e+s^d)}} e^{-jks^d} . \tag{36a}$$

The $\bar{\bar{D}}_e$ in (36a) can also be expressed as

$$\bar{\bar{D}}_e = -\hat{\beta}_0'\hat{\beta}_0 D_{es} - \hat{\phi}'\hat{\phi} D_{eh} . \tag{36b}$$

In matrix notation, (36a) becomes

$$\begin{bmatrix} E^d_{\beta_0} \\ E^d_{\phi} \end{bmatrix} = \begin{bmatrix} -D_{es} & 0 \\ 0 & -D_{eh} \end{bmatrix} \begin{bmatrix} E^i_{\beta_0'} \\ E^i_{\phi'} \end{bmatrix} \sqrt{\frac{\rho_e}{s^d(\rho_e+s^d)}} e^{-jks^d} \tag{37}$$

in which the D_{es} and D_{eh} are [13]:

$$D_{\substack{e\\h}}(\phi,\phi';\beta_o) = \frac{-e^{-j\frac{\pi}{4}}}{2n\sqrt{2\pi k}\sin\beta_o}\left[\cot\left(\frac{\pi+(\phi-\phi')}{2n}\right)F[kL^i a^+(\phi-\phi')] + \cot\left(\frac{\pi-(\phi-\phi')}{2n}\right)F[kL^i a^-(\phi-\phi')]\right.$$

$$\left.\mp\left[\cot\frac{\pi+(\phi+\phi')}{2n}F[kL^{rn}a^+(\phi+\phi')] + \cot\frac{\pi-(\phi+\phi')}{2n}F[kL^{ro}a^-(\phi+\phi')]\right]\right] \quad (38)$$

where the asymptotic large parameter kL (with the superscripts i, rn, ro on L omitted for convenience) is required to be sufficiently large (generally greater than 3) and

$$a^{\pm}(\beta) = 2\cos^2\left(\frac{2n\pi N^{\pm} - (\beta)}{2}\right) \quad . \quad (39a)$$

The $N^{\pm}$ are the integers which most nearly satisfy the equation:

$$2\pi n N^{\pm} - \beta = \pm\pi \quad (39b)$$

with

$$\beta = \phi \pm \phi' \; . \quad (39c)$$

Note that n=2 for a half plane or a semi-infinite curved screen. Also, n=3/2 for an exterior right angled wedge, etc.

For exterior edge diffraction N^+=0 or 1, and N^-=-1, 0, or 1. The values of $N^{\pm}$ at the shadow and reflection boundaries as well as their associated transition regions are given in Table I for exterior wedge angles (1 < n < 2):

TABLE I

	The cotangent is singular when	value of N at the boundary
$\cot\left(\frac{\pi+(\phi-\phi')}{2n}\right)$	$\phi = \phi'-\pi$, an ISB surface ϕ=0 is shadowed	$N^+ = 0$
$\cot\left(\frac{\pi-(\phi-\phi')}{2n}\right)$	$\phi = \phi'+\pi$, an ISB surface $\phi=n\pi$ is shadowed	$N^- = 0$
$\cot\left(\frac{\pi+(\phi+\phi')}{2n}\right)$	$\phi = (2n-1)\pi-\phi'$, an RSB reflection from surface $\phi=n\pi$	$N^+ = 1$
$\cot\left(\frac{\pi-(\phi+\phi')}{2n}\right)$	$\phi = \pi-\phi'$, an RSB reflection from surface ϕ=0	$N^- = 0$

For a point source (or spherical wave) type illumination, the distance parameter L^i is:

$$L^i = \frac{s^i s^d}{s^i+s^d}\sin^2\beta_o \quad , \quad (40)$$

in which s^i and s^d are the distances from the point of edge diffraction at Q_E to the source and observation points, respectively. Only for a straight wedge with planar faces that is illuminated by a point source,

$$L^{ro} = L^{rn} = L^i = \frac{s^i s^d}{s^i+s^d}\sin^2\beta_o \quad (41)$$

as in (40). For an arbitrary ray optical illumination which is characterized by two distinct principal wavefront radii of curvature, ρ_1^i and ρ_2^i, the above L^i must be modified as shown below in the general expressions for L^{ro} and L^{rn} pertaining to a curved wedge; thus,

$$L^i = \left[\frac{s^d(\rho_e^i+s^d)\rho_1^i\rho_2^i\sin^2\beta_o}{\rho_e^i(\rho_1^i+s^d)(\rho_2^i+s^d)}\right]_{\text{at ISB}} \quad ; \quad (42a)$$

$$L^r = \left[\frac{s^d(\rho_e^r+s^d)\rho_1^r\rho_2^r\sin^2\beta_o}{\rho_e^r(\rho_1^r+s^d)(\rho_2^r+s^d)}\right]_{\text{at RSB}} \quad . \tag{42b}$$

Here, L^{ro} and L^{rn} are the values of L^r associated with the "0" and "n" faces of the wedge, respectively. Furthermore, ρ_e^r is given by:

$$\frac{1}{\rho_e^r} = \frac{1}{\rho_e^i} - \frac{2(\hat{n}\cdot\hat{n}_e)(\hat{s}^i\cdot\hat{n})}{a\sin^2\beta_o} \quad . \tag{43a}$$

Also ρ_e in (36) is given by:

$$\frac{1}{\rho_e} = \frac{1}{\rho_e^i} - \frac{\hat{n}_e\cdot(\hat{s}^i-\hat{s}^d)}{a\sin^2\beta_o} \quad . \tag{43b}$$

The unit vector $\hat{n}$ is defined in Figure 8(b); whereas, $\hat{n}_e$ is a unit vector normal to the edge which is directed away from the center of edge curvature at Q_E. The radius of edge curvature is denoted by "a" in (43). ρ_e^i is the radius of curvature of the incident wavefront at Q_E which lies in the edge fixed plane of incidence. In the far zone when $s^d \gg \rho_{1,2}^i$, $s^d \gg \rho_{1,2}^r$, and $s^d \gg \rho_e$ then the L^i and L^r in (42a) and (42b) simplify to $L = \frac{\rho_1\rho_2\sin^2\beta_o}{\rho_e}$ in which the appropriate superscripts on L, ρ_1 and ρ_2 are omitted for convenience. It is noted that L^i and L^r in (42a) and (42b) are calculated on the appropriate shadow boundaries. The transition function, F which appears in (38) contains a Fresnel integral; it is defined by

$$F(x) = 2j\sqrt{x}\; e^{jx}\int_{\sqrt{x}}^{\infty} d\tau\, e^{-j\tau^2} \quad . \tag{44}$$

A plot of the above F(x) is illustrated in Figure 13. In (44), $\sqrt{x} = |\sqrt{x}|$ if $x>0$ and $\sqrt{x} = -j\,|\sqrt{x}|$ if $x<0$. If $x<0$, then $F(x)\big|_{x<0} = F^*(|x|)$ where * denotes the complex conjugate. Exterior to the $\binom{ISB}{RSB}$ transition regions x becomes large and $F(x)\to 1$ so that the uniform $D_{\substack{es\\eh}}$ in (38) then reduces to Keller's form as it should; namely,

$$\tilde{D}_e \to \tilde{D}_e^k, \text{ outside the transition region.} \tag{45}$$

Near the (ISB and RSB) boundaries, the small argument approximation for F(x) may be employed (since x = o on ISB and RSB); namely, one can incorporate

$$F(x) \underset{x\to o}{\to} \sqrt{\pi x}\; e^{j(\frac{\pi}{4}+x)} \tag{46}$$

into (38) to arrive at the following result for the diffracted field $\bar{E}^d$ at ISB or RSB:

$$\bar{E}^d\Big|_{ISB;RSB} = \left[\mp\frac{1}{2}\bar{E}^{i;r} + \begin{pmatrix}\text{continuous}\\ \text{higher order}\\ \text{terms}\end{pmatrix}\right] , \tag{47}$$

$$\text{if } \begin{cases}\text{on lit side of ISB;RSB}\\ \text{on shadow side of ISB;RSB}\end{cases}$$

The above result in (47) ensures the continuity of the total HF field in (24) at ISB and RSB. The field contribution arising from the edge excited "surface diffracted rays" is not included in (24); it may be important for observation points close to the surface shadow boundaries (SSB) associated with the tangent to the "0" and "n" faces of a curved wedge at Q_E if the "0" and "n" faces are convex boundaries. The result in (36a) and (36b) along with (38) is valid away from any diffracted ray caustics and away from the edge caustic at Q_E.

For grazing angles of incidence on a wedge with planar faces, $D_{es} = o$, and D_{eh} must be replaced by $(^1/_2)$ D_{eh}. The reason for the $^1/_2$ factor in the latter case is explained as follows. The incident and reflected GO fields tend to combine into a single "total incident field" as one approaches grazing angles of incidence; consequently, only half of this "total field" illuminating the edge at grazing constitutes the incident GO field while the other half constitutes the reflected GO field. The case of grazing angles of incidence at an edge in a curved surface cannot be handled as easily as the case of a wedge with planar faces. Presently, one can only treat angles of incidence that are greater than $\left[\frac{2}{k\rho_g(Q_E)}\right]^{1/3}$ where $\rho_g(Q_E)$ is the radius of curvature of the surface in the direction of the incident ray at the point of edge diffraction Q_E.

Under the above restrictions, the result in (38) for $D_{\substack{es\\eh}}$ simplifies in the case of a plane or curved screen (n=2 case) to

$$D_{\substack{es\\eh}}(\phi,\phi',\beta_o) = \frac{-e^{-j\frac{\pi}{4}}}{2\sqrt{2\pi k}\,\sin\beta_o}\left[\sec\left(\frac{\phi-\phi'}{2}\right)F[kL^i a(\phi-\phi')] \mp \sec\left(\frac{\phi+\phi'}{2}\right)F[kL^r a(\phi+\phi')]\right] \tag{48}$$

where $a(\beta)=2\cos^2(\beta/2)$ and $L^{i,r}$ are in (42a;b) with the understanding that L^r is evaluated at the RSB corresponding to the face which is illuminated; hence the superscripts "o" and "n" in L^r are dropped for this n=2 case.

The edge diffracted field $\bar{E}^d(P)$ for the 2-D situation can be obtained from (36a) by allowing ρ_e to approach infinity and by requiring $\beta_o = \pi/2$; thus, for the 2-D case,

$$\bar{E}^d(P) = \bar{E}^i(Q_E)\cdot\bar{\bar{D}}_e(\phi,\phi',\pi/2;\,k)\,\frac{e^{-jks^d}}{\sqrt{s^d}} \quad . \tag{49}$$

The $\bar{\bar{D}}_e$ in (49) for the 2-D case is available from (36a) and (36b) with $\beta_o=\pi/2$ (or $\sin\beta_o = 1$). Also, L^i for the 2-D case is given by (41) with $\beta_o = \pi/2$; in particular,

$$L^i = \frac{s^i s^d}{s^i + s^d} \quad . \tag{50}$$

Likewise, L^r is obtained from (42b) with $\beta_o = \pi/2$, $\rho_1^r \to \infty$, $\rho_2^r \equiv \rho^r$ (as in (22)), and $\rho_e^r \to \infty$; therefore, in the 2-D case

$$L^r = \frac{\rho^r s^d}{\rho^r + s^d} \quad . \tag{51}$$

Note that ρ^r in (51) is the same as the one in (23); however, ρ^r is in general different for the "O" and "n" faces of the wedge, with L^{ro} and L^{rn} denoting the values of L^r for these two different faces. While the expression for L^r in (42b) is fixed to its value on the RSB for convenience, the one in (51) can be evaluated as a function of the observation point with almost the same ease as if one had approximated the value of L^r by its value at the RSB. The values of L^i and L^r for the 3-D case involve various caustic distances as is evident from (42a) and (42b). These distances are generally slowly varying within the ISB and RSB transition regions and it is therefore convenient to approximate L^i and L^r throughout the transition regions by their values at the ISB and RSB as done in (42a) and (42b). Outside the respective transition regions, the F functions containing L^i and L^r approach unity anyway unaffected by the above approximation.

It is noted that the comment below (47) in regard to grazing incidence is also valid for the 2-D case. It is further noted that the essential difference between $\bar{\bar{D}}_e$ and $\bar{\bar{D}}_e^k$ is that the former is range dependent whereas the latter is not. As a result, (36a) is not ray optical within the ISB and RSB transition regions; exterior to these regions, $\bar{\bar{D}}_e \to \bar{\bar{D}}_e^k$ as indicated before. Figure 9 illustrates the diffraction of a plane wave by a perfectly-conducting half-plane. It is noted that the geometrical optics field is discontinuous; however, the UTD diffracted field cancels the GO discontinuity to yield a total UTD field which is continuous.

(ii) <u>Diffraction at a Smooth Convex Surface</u>

The geometry for this problem of the diffraction by a smooth convex surface is shown in Figure 10. The total high frequency field $\bar{E}(P)$ for the situation in Figure 10 can be written as

$$\bar{E}(P) = \begin{cases} \bar{E}^i(P_L)U + \bar{E}^r(P_L)U + \bar{E}^d(P_L) & \text{, if } P = P_L \text{ in the lit zone.} \\ \bar{E}^d(P_S)\,[1 - U] & \text{, if } P = P_S \text{ in the shadow zone.} \end{cases} \tag{52}$$

The incident and reflected fields $\bar{E}^i$ and $\bar{E}^r$ are associated with the incident and reflected GO rays shown in Figure 11. The step function U in (52) is defined below with respect to the surface shadow boundary (SSB) as:

$$U = \begin{cases} 1, \text{ in the lit region which lies above the SSB} \\ 0, \text{ in the shadow region which lies below the SSB,} \end{cases} \tag{53}$$

The surface diffracted field $\bar{E}^d(P_S)$ follows the surface diffracted ray path into the shadow region, as in Figure 11; whereas, the field $\bar{E}^d(P_L)$ which is diffracted into the lit region follows the reflected ray path (of $\bar{E}^r$) in this solution. Therefore, it is convenient in this problem to combine the GO reflected field $\bar{E}^r(P_L)U$ and the diffracted field $\bar{E}^d(P_L)$ into a single "generalized reflected field", $\bar{E}^{gr}(P_L)U$ in the lit region so that (52) becomes

$$\bar{E}(P) = \begin{cases} \bar{E}^i(P_L)U + \bar{E}^{gr}(P_L)U & , \text{ if } P = P_L \text{ in the lit zone.} \\ \bar{E}^d(P_S)\,[1 - U] & , \text{ if } P = P_S \text{ in the shadow zone.} \end{cases} \tag{54}$$

The fields $\bar{E}^{gr}(P_L)$ and $\bar{E}^d(P_S)$ are given symbolically by

$$\bar{E}^{gr}(P_L) \sim \bar{E}^i(Q_R)\cdot[\mathcal{R}_s\hat{e}_\perp\hat{e}_\perp + \mathcal{R}_h\hat{e}^i_\parallel\hat{e}^r_\parallel]\sqrt{\frac{\rho_1^r\rho_2^r}{(\rho_1^r+s^r)(\rho_2^r+s^r)}}\; e^{-jks^r} , \tag{55}$$

$$\bar{E}^d(P_S) \sim \bar{E}^i(Q_1)\cdot[\mathcal{D}_s\hat{b}_1\hat{b}_2 + \mathcal{D}_h\hat{n}_1\hat{n}_2]\sqrt{\frac{\rho_s}{s^d(\rho_s+s^d)}}\; e^{-jks^d} , \tag{56}$$

where the points Q_R and Q_1, and the distances s^r and s^d are indicated in Figure 10. The surface diffracted ray caustic distance ρ_s is shown in Figure 11. The quantities within brackets involving $\mathcal{R}_{s,h}$ and $\mathcal{D}_{s,h}$ in (55) and (56) may be viewed as generalized dyadic coefficients for surface reflection and diffraction, respectively. It is noted that (55) and (56) are expressed invariantly in terms of the unit vectors fixed in the reflected and surface diffracted ray coordinates. The unit vectors $\hat{e}^i_\parallel$, $\hat{e}^r_\parallel$, and $\hat{e}_\perp$ in (55) have been defined earlier in connection with the reflected field. It can be shown that cross terms actually exist in the above generalized dyadic reflection coefficient; but, in general their effect is seen to be weak within the SSB transition region. Also these terms vanish in the deep lit region and on the SSB, hence they have been ignored in (55).

At Q_1, let $\hat{t}_1$ be the unit vector in the direction of incidence, $\hat{n}_1$ be the unit outward normal vector to the surface, and $\hat{b}_1 = \hat{t}_1 \times \hat{n}_1$; likewise at Q_2, let a similar set of unit vectors $(\hat{t}_2, \hat{n}_2, \hat{b}_2)$ be defined with $\hat{t}_2$ in the direction of the diffracted ray as in Figure 12. In the case of surface rays with zero torsion, $\hat{b}_1 = \hat{b}_2$. It is clear from Figure 11 that ρ_s in (56) is the wave-front radius of curvature of the surface diffracted ray evaluated in the $\hat{b}_2$ direction at Q_2. First, the UTD expressions for $\mathcal{R}_{s,h}$ and $\mathcal{D}_{s,h}$ in (55) and (56) will be given below; it will be shown that these expressions are valid within the transition region adjacent to the SSB. Subsequently, it will be shown how these expressions automatically simplify outside the SSB transition region to reduce to those obtained by Keller in his GTD representation. The $\mathcal{R}_{s,h}$ and $\mathcal{D}_{s,h}$ in (55) and (56) are [14,15]:

$$\mathcal{R}_{\substack{s\\h}} = -\left[\sqrt{\frac{-4}{\xi^L}}\; e^{-j(\xi^L)^3/12}\left[-\frac{e^{-j\pi/4}}{2\sqrt{\pi}\,\xi^L}[1-F(X^L)] + \tilde{P}_{\substack{s\\h}}(\xi^L)\right]\right] \quad , \text{ for the lit region} \tag{57}$$

and

$$\mathcal{D}_{\substack{s\\h}} = -\left[\sqrt{m(Q_1)m(Q_2)}\sqrt{\frac{2}{k}}\;\frac{e^{-j\frac{\pi}{4}}}{2\sqrt{\pi}\,\xi}\;[1-F(X^d)] + \tilde{P}_{\substack{s\\h}}(\xi)\right]\sqrt{\frac{d\eta(Q_1)}{d\eta(Q_2)}}\; e^{-jkt} \quad , \text{ for the shadow region} \tag{58}$$

TABLE II

Zeros of the Airy Function	Zeros of the Derivative of the Airy Function
$Ai(-q_p)=0$	$Ai'(-\bar{q}_p) = 0$
$q_1 = 2.33811$	$\bar{q}_1 = 1.01879$
$q_2 = 4.08795$	$\bar{q}_2 = 3.24820$
$Ai'(-q_1) = 0.70121$	$Ai(-\bar{q}_1) = 0.53566$
$Ai'(-q_2) = -0.80311$	$Ai(-\bar{q}_2) = -0.[illegible]02$

The function F appearing above has been defined earlier in (44). The Fock type surface reflection function $\tilde{P}_{\substack{s\\h}}$ is related to the $\binom{\text{soft}}{\text{hard}}$ Pekeris function $\binom{p^*}{q^*}$ by

$$\tilde{P}_{\substack{s\\h}}(\delta) = \begin{Bmatrix} p^*(\delta) \\ q^*(\delta) \end{Bmatrix} e^{-j\frac{\pi}{4}} - \frac{e^{-j\frac{\pi}{4}}}{2\sqrt{\pi}\delta} \quad , \text{ (Note that } \delta=0 \text{ at SSB)} \tag{59a; 59b}$$

where p* and q* are finite and well behaved even when $\delta=0$; these universal functions are plotted in Figures 13, 14 and 15. Also,

$$\tilde{P}_{\substack{s\\h}}(\delta) = \frac{e^{-j\frac{\pi}{4}}}{\sqrt{\pi}} \int_{-\infty}^{\infty} d\tau \, \frac{\tilde{\partial}V(\tau)}{\tilde{\partial}W_2(\tau)} e^{-j\delta\tau} \;;\; \tilde{\partial} = \begin{cases} 1 & \text{, soft case} \\ \frac{\partial}{\partial\tau} & \text{, hard case} \end{cases} \tag{60a; 60b}$$

in which the Fock type Airy functions $V(\tau)$ and $W_2(\tau)$ are

$$2jV(\tau) = W_1(\tau) - W_2(\tau) \;;\; W_1(\tau) = \frac{1}{\sqrt{\pi}} \int_{-\infty}^{\infty e^{-j2\pi/3}} dt \, e^{\tau t - t^3/3} \;; \tag{61a;61b}$$

$$W_2(\tau) = \frac{1}{\sqrt{\pi}} \int_{-\infty}^{\infty e^{j2\pi/3}} dt \, e^{\tau t - t^3/3} \quad . \tag{61c}$$

The rest of the quantities occurring in (57) and (58) are:

$$\xi^L = -2m(Q_R)\cos\theta^i \;;\; \xi = \int_{Q_1}^{Q_2} dt' \, \frac{m(t')}{\rho_g(t')} \;;\; m(\cdot) = \left[\frac{k\rho_g(\cdot)}{2}\right]^{1/3} \tag{62;63;64}$$

$$t = \int_{Q_1}^{Q_2} dt' \;;\; X^L = 2kL\cos^2\theta^i \;;\; X^d = \frac{kL(\xi)^2}{2m(Q_1)m(Q_2)} \quad . \tag{65;66;67}$$

The quantity $\rho_g(Q_R)$ in $m(Q_R)$ denotes the surface radius of curvature at Q_R in the plane of incidence; whereas, $\rho_g(Q_{\substack{1\\2}})$ is the surface radius of curvature at $Q_{\substack{1\\2}}$ in the $\hat{t}_{\substack{1\\2}}$ direction. The dt' in (63) and (65) is an incremental arc length along the surface ray path. The angle of incidence θ^i is shown in Figure 6. Also, the $d\eta(Q_1)$ and $d\eta(Q_2)$ in (58) denote the widths of the surface ray tube at Q_1 and Q_2, respectively; the surface ray tube is formed by considering a pair of rays adjacent to the central ray as in Figure 11. The geodesic surface ray paths are easy to find on cylinders, spheres, and cones. For example, the geodesic paths on a convex cylinder are helical; whereas, they are great circle paths on a sphere. For more general convex surfaces, the geodesic surface ray paths must be found numerically. The distance parameter L in (66) and (67) is given by

$$L = \frac{\rho_1^i(Q_1)\;\rho_2^i(Q_1)}{(\rho_1^i(Q_1)+s)(\rho_2^i(Q_1)+s)} \cdot \frac{s(\rho_b^i(Q_1)+s)}{\rho_b^i(Q_1)} \quad , \tag{68}$$

where:

$$s = \left(s^r\Big|_{SSB} = s^d\Big|_{SSB}\right) \;;\; \rho_b^i(Q_1) = \begin{cases} \text{incident wavefront radius of curvature} \\ \text{in the } \hat{b}_1 \text{ direction at } Q_1 \end{cases} \tag{69;70}$$

The distance s in (68) may be obtained by projecting $\binom{s^r}{s^d}$ on the SSB if the observation point within the $\binom{\text{lit}}{\text{shadow}}$ side of the SSB transition region does not move in a predetermined manner. If the observation point moves across the SSB in a predetermined fashion then it is clear that s in (68;69) can be found unambiguously. The $\rho_1^i(Q_1)$ and $\rho_2^i(Q_1)$ in (68) denote the principal radii of curvature of the incident wavefront at Q_1, and ρ_b^i, which is defined in (70), has been introduced earlier in (18b). For the special case of point source or spherical wave illumination, the L in (66) and (67) simplifies to:

$$L = \frac{s's}{s'+s} \quad , \text{ for spherical wave illumination,} \tag{71}$$

where:

$$s' \equiv \left(\rho_1^i(Q_1) = \rho_2^i(Q_1) = \rho_b^i(Q_1)\right) = \text{distance from the point source to the point of grazing incidence at } Q_1. \tag{72}$$

In the case of <u>plane wave illumination</u>, $s' \to \infty$ and hence (71) above simplifies to:

$$L = s \quad , \text{ for plane wave illumination.} \tag{73}$$

If the incident wavefront is of the converging $\rho^i_{1,2} < 0$, or converging-diverging ($\rho^i_1 \gtrless 0$; $\rho^i_2 \lessgtr 0$) type, then the parameter L in (68) can become negative. It has not been fully investigated how the general solution can be completed if L becomes negative. On the other hand, if one of the principal directions of the incident wavefront coincides with one of the principal planes of the surface at grazing, then one can treat a converging, or converging-diverging (saddle) type wavefront for which $L<0$, by replacing $F(X^{L,d})$ with $F^*(|X^{L,d}|)$. Note that the asterisk on F^* denotes the complex conjugate operator. The use of $F^*(|X^{L,d}|)$ when $L<0$ leads to a continuous total field at SSB in this case.

The above UTD result remains accurate outside the paraxial (i.e. near axial) regions of quasi-cylindrical or elongated convex surfaces; a different solution is required in these regions and it has not yet been completed. It is assumed that the source and observation points are not too close to the surface. Also, it is assumed that any caustics of the incident ray system are not too close to the surface. Furthermore, the amplitude of the incident field is assumed to be slowly varying at Q_1 and Q_1; otherwise, it is necessary to add a slope diffraction contribution. The UTD solution described above remains accurate if kL and m are sufficiently large. Typically kL should be larger than 3 although in some cases kL can be made smaller. Also m should be such that $2m^3>5$ or so; however, the results generally lose their accuracy slowly as $2m^3$ becomes smaller. It is noted that the angular extent of the SSB transition region is of order m^{-1} radians.

A surface diffracted field of the type $\bar{E}^d(P_s)$ can also be present in the lit zone if the surface is closed; this may be seen by noting that the field of the type $\bar{E}^d$ can propagate around the closed surface. Also, additional contributions to $\bar{E}^d(P_s)$ can be present in the shadow zone for a closed surface because surface diffracted rays can be initiated at all points of grazing incidence on that closed surface; furthermore, these surface rays can undergo multiple encirclements around the closed body. However, these additional surface diffracted ray contributions are generally quite weak in comparison to the $\bar{E}^{gr}$ contribution within the lit zone for surfaces which are quite large in terms of the wavelength; hence their contribution may be neglected in such cases.

The parameters ξ^L, ξ, X^L and X^d become small as one approaches the surface shadow boundary, SSB, from both the lit and shadow regions. As one approaches the SSB, the small argument limiting form of the transition function F(X) which has been introduced previously in (44) becomes helpful for verifying the continuity of the total high frequency field at the SSB. On the other hand, the above parameters become large as one moves outside the SSB transition region; in this case $F(X)\to 1$ for large X, and likewise,

$$\tilde{P}_{\substack{s\\h}}(\delta)\Big|_{\delta<<0} \sim \pm \sqrt{\frac{-\delta}{4}}\; e^{j\delta^3/12} \tag{74}$$

$$\tilde{P}_{\substack{s\\h}}(\delta)\Big|_{\delta>>0} = \begin{cases} -\dfrac{e^{-j\pi/4}}{\sqrt{\pi}} \displaystyle\sum_{n=1}^{N} \dfrac{e^{j\pi/6}\, e^{\delta q_n e^{-j5\pi/6}}}{2[Ai'(-q_n)]^2} \\[2ex] -\dfrac{e^{-j\pi/4}}{\sqrt{\pi}} \displaystyle\sum_{n=1}^{N} \dfrac{e^{j\pi/6}\, e^{\delta \bar{q}_n e^{-j5\pi/6}}}{2[\bar{q}_n][Ai(-\bar{q}_n)]^2} \end{cases} \tag{75}$$

where N = 2 is generally sufficient to compute $\tilde{P}_{\substack{s\\h}}(\delta)$ accurately for $\delta>>0$ in (75). In (75) and Table II, the Miller type Airy function $Ai(\tau) = V(\tau)/\sqrt{\pi}$, and $Ai'(\tau) = \frac{d}{d\tau} Ai(\tau)$. Thus, upon incorporating the limiting values of (74) and (75), which are valid outside the SSB transition region, into (57) and (58) and replacing F(X) by it's asymptotic value of unity, it is clear that $\mathcal{R}_s$ reduces to $R_{\substack{s\\h}} = \mp 1$ outside the SSB transition region so that $\bar{E}^{gr}(P_L) \to \bar{E}^r(P_L)$ of GO, and likewise $\bar{E}^d(P_s) \to \bar{E}^d_k(P_s)$ therein, respectively, in which the Keller surfaced diffracted ray field $\bar{E}^d_k(P_s)$ is given by [3]

$$\bar{E}^d_k(s) \sim \bar{E}^i(Q_1) \cdot \bar{\bar{T}}^k(Q_1,Q_2)\, e^{-jkt} \sqrt{\frac{dn(Q_1)}{dn(Q_2)}} \sqrt{\frac{\rho_s}{s^d(\rho_s+s^d)}}\; e^{-jks^d} \tag{76}$$

$$\bar{\bar{T}}^k(Q_1,Q_2) = \left[\hat{b}_1\, \hat{b}_2\, T_s + \hat{n}_1\, \hat{n}_2\, T_n\right] \quad , \tag{77}$$

where

$$T_{\substack{s\\h}} = \sum_{n=1}^{N} D^{\substack{s\\h}}_n(Q_1)\, e^{-\int_{Q_1}^{Q_2} \alpha^{\substack{s\\h}}_n(t')dt'}\, D^{\substack{s\\h}}_n(Q_2) \quad . \tag{78}$$

The $D_n^{\hat{s}}$ and $\alpha_n^{\hat{s}}$ are the Keller's GTD diffraction coefficients and attenuation constants for the n^{th} soft (s) or hard (h) surface ray mode. Thus, in the GTD, the surface ray field consists of surface ray modes which propagate independently of one another. Also, this surface ray field is not the true field on the surface; it is a boundary layer field. The $D_n^{\hat{s}}$ and $\alpha_n^{\hat{s}}$ are given by:

$$[D_n^s(Q)]^2 = \sqrt{\frac{1}{2\pi k}}\; m(Q)\, \frac{e^{-j(\pi/12)}}{[Ai'(-q_n)]^2} \quad ; \tag{79a}$$

$$[D_n^h(Q)]^2 = \sqrt{\frac{1}{2\pi k}}\; m(Q)\, \frac{e^{-j(\pi/12)}}{\bar{q}_n[Ai(-\bar{q}_n)]^2} \quad , \tag{79b}$$

and

$$\alpha_n^s(Q) = \frac{q_n}{\rho_g(Q)}\; m(Q) e^{j(\pi/6)} \quad ; \quad \alpha_n^h = \frac{\bar{q}_n}{\rho_g(Q)}\, m(Q) e^{j(\pi/6)} \quad . \tag{80a;80b}$$

In (79) - (80), Q is any point on the geodesic surface ray path. The GTD result of (76) in terms of (77) and (78) is not valid within the SSB transition region.

The UTD result for the 3-D configuration can be simply modified to recover the corresponding UTD result for the 2-D case by allowing the caustic distances ρ_1^r and ρ_s in (55) and (56) to receed to infinity. Then, let

$$\rho_2^r \equiv \rho^r, \text{ if } \rho_1^r \to \infty \text{ and } \rho_s \to \infty \quad , \tag{81}$$

so that

$$\bar{E}^{gr}(P_L) \sim \bar{E}^i(Q_R) \cdot [\mathcal{R}_s\, \hat{e}_\perp \hat{e}_\perp + \mathcal{R}_h\, \hat{e}_{//}^i \hat{e}_{//}^r] \sqrt{\frac{\rho^r}{\rho^r + s^r}}\, e^{-jks^r} \tag{82}$$

in which ρ^r is as in (23), and

$$\bar{E}^d(P_s) \sim \bar{E}^i(Q_1) \cdot [\mathcal{D}_s\, \hat{b}\hat{b} + \mathcal{D}_h\, \hat{n}_1 \hat{n}_2]\; \frac{e^{-jks^d}}{\sqrt{s^d}} \quad , \tag{83}$$

since $(\hat{b}_1 = \hat{b}_2 \equiv \hat{b}$ for the 2-D case (note: $\hat{b} = \hat{e}_\perp$)). The $\mathcal{R}_{\substack{s\\h}}$ and $\mathcal{D}_{\substack{s\\h}}$ in (82) and (83) are as defined earlier, respectively; only the L appearing in (66) and (67) is given by

$$L = \frac{s's^d}{s'+s^d} \quad , \text{ for the 2-D case,} \tag{84}$$

where s' is the distance from the 2-D line source to the point of grazing incidence at Q_1 and $s \equiv s^d\big|_{SSB}$ as before. A comparison of the UTD and GTD solutions for a 2-D circular cylinder illuminated by a nearby line source is illustrated in Figures 16(a) and 16(b); those UTD solutions are then compared with the corresponding exact (Eigenfunction) solutions in Figures 17(a) and 17(b).

III. A FEW ADDITIONAL UTD SOLUTIONS AND SOME APPLICATIONS

In addition to the basic UTD edge and convex surface diffraction solutions described above, UTD solutions for some other canonical shapes also exist; however, the latter are not described here because of space limitations. UTD type solutions for the radiation and mutual coupling associated with antennas on a smooth convex surface are given in [16-19]; also, an approximate vertex diffraction solution may be found in [5,11,20]. A result based on a recently obtained approximate UTD solution for the field scattered by a fully illuminated, semi-infinite, right-circular perfectly-conducting cone [21] is shown in Figure 18. Also, UTD results for the 3-D diffraction by a penetrable dielectric/ferrite strip in Figure 19 based on the work in [22] are shown in Figures 20 and 21, for parallel and perpendicular polarization of the incident field, respectively. It is noted therein that even though the incident fields are TE_z or TM_z, the scattered fields are not simply TE_z or TM_z due to a coupling between the two which is introduced by the dielectric edge when $\theta' \neq \pi/2$. Finally, Figures 22 and 23 show the application of UTD to deal with more realistic shapes [23,24]. The ogival shape in Figure 22 has a circular duct on it. In Figure 23, the aircraft fuselage is modeled by a best fit prolate spheroid near the antenna location, a more recent calculation employs a composite ellipsoid fuselage model [25].

Acknowledgement
This work was sponsored by the Joint Services Electronics Program under Contract No. N00014-78-C-0049 with the Ohio State University Research Foundation.

REFERENCES

[1] J.B. Keller, "Geometrical Theory of Diffraction," J. Opt. Soc. Am., Vol. 52, pp. 116-130, 1962.

[2] J.B. Keller, "A Geometrical Theory of Diffraction," in Calculus of Variations and Its Applications, L.M. Graves, Ed., New York, McGraw-Hill, pp. 27-52, 1958.

[3] B.R. Levy and J.B. Keller, "Diffraction by a smooth Object," Comm. Pure and Appl. Math., Vol. 12, pp. 159-209, 1959.

[4] R.G. Kouyoumjian, "The Geometrical Theory of Diffraction and Its Applications," in Numerical and Asymptotic Techniques in Electromagnetics, R. Mittra, ed., New York, Springer-Verlag, 1975.

[5] R.G. Kouyoumjian, P.H. Pathak, and W.D. Burnside, "A Uniform GTD for the Diffraction by Edges, Vertices, and Convex Surfaces," in Theoretical Methods for Determining the Interaction of Electromagnetic Waves with Structures, J.K. Skwirzynski, ed., Netherlands, Sijthoff and Noordhoff, 1981.

[6] S.W. Lee and G.A. Deschamps, "A Uniform Asymptotic Theory of EM Diffraction by a Curved Wedge," IEEE Trans. AP-24, pp. 25-34, January 1976. Also see D.S. Ahluwalia, R.M. Lewis, and J. Boersma, "Uniform asymptotic theory of diffraction by a plane screen," SIAM J. Appl. Math., Vol. 16, pp. 783-807, 1968.

[7] C.E. Ryan Jr. and L. Peters, Jr., "Evaluation Edge Diffracted Fields Including Equivalent Currents for Caustic Regions," IEEE Trans. AP-7, pp. 292-299, 1969.

[8] W.D. Burnside and L. Peters, Jr., "Axial RCS of Finite Cones by the Equivalent Current Concept with Higher Order Diffraction," Radio Sci., Vol. 7, #10, pp. 943-948, Oct. 1972.

[9] E.F. Knott and T.B.A. Senior, "Comparison of Three High-Frequency Diffraction Techniques," Proc. IEEE, Vol. 62, pp. 1468-1474, 1974.

[10] P. Ya. Ufimtsev, "Method of edge waves in the physical theory of diffraction," (from the Russian "Method Krayevykh voln v fizicheskoy teorii difraktsii," Izd-Vo Sov. Radio, pp. 1-243 (1962), translation prepared by the U.S. Air Force Foreign Technology Division, Wright-Patterson AFB, Ohio; released for public distribution Sept. 7, 1971.

[11] P.H. Pathak, "Techniques for High Frequency Problems," chapter in Handbook of Antenna Theory and Design, (eds., Y.T. Lo and S.W. Lee), to be published in 1987 by Van Nostrand (Cat. No. 22054).

[12] S. Silver, Microwave Antenna Theory and Design, Boston Technical Publishers, Inc., 1964.

[13] R.G. Kouyoumjian and P.H. Pathak, "A Uniform Geometrical Theory of Diffraction for an Edge in A Perfectly Conductin Surface:, Proc. IEEE, Vol. 62, pp. 1448-1461, November 1974.

[14] P.H. Pathak: "An Asymptotic Result for the Scattering of a Plane Wave by a Smooth Convex Cylinder," J. Radio Science, Vol. 14, No. 3, pp. 419-435, May-June 1979.

[15] P.H. Pathak, W.D. Burnside and R.J. Marhefka: "A Uniform GTD Analysis of the Diffraction of Electromagnetic Waves by a Smooth Convex Surface," IEEE Trans. Antennas and Propagation, Vol. AP-28, No. 5, pp. 631-642, September 1980.

[16] P.H. Pathak, N. Wang, W.D. Burnside and R.G. Kouyoumjian: "Uniform GTD Solution for the Radiation from Sources on a Smooth Convex Surface," IEEE Trans, Antennas and Propagation, Vol. AP-29, No. 4, pp. 609-621, July 1981.

[17] P.H. Pathak and N.N. Wang: "Ray Analysis of Mutual Coupling Between Antennas on A Convex Surface," IEEE Trans. Antennas and Propagation, Vol. AP-29, No. 6, pp. 911-922, November 1981.

[18] S.W. Lee, "Mutual Admittance of Slots on a Cone: Solution by Ray Technique," IEEE Trans. Antennas Propagat., Vol. AP-26, no. 6, pp. 768-773, Nov. 1978.

[19] K.K. Chan, L.B. Felsen, A. Hessel and J. Shmoys, "Creeping Waves on a Perfectly-Conducting Cone," IEEE Trans. AP-26, pp. 661-670, Sept. 1977.

[20] F.A. Sikta, W.D. Burnside, T.T. Chu and L. Peters, Jr., "First-order equivalent current and corner diffraction scattering from flat plate structures," IEEE Trans. Antennas and Prop., Vol. 31, No. 4, pp. 584-589, July 1983.

[21] K.D. Trott, "A High Frequency Analysis of Electromagnetic Plane Wave Scattering by a Fully Illuminated Perfectly-Conducting Semi-Infinite Cone," Ph.D. dissertation, The Ohio State University, Department of Electrical Engineering, Columbus, Ohio, Summary 1986.

[22] R.G. Rojas, "A Uniform GTD Analysis of the EM Diffraction by a Thin Dielectric/Ferrite Half-Plane and Related Configurations," Ph.D. dissertation, The Ohio State University, Department of Electrical Engineering, Columbus, Ohio, Winter 1985.

[23] J. Volakis, "EM Scattering from Inlets and Plates Mounted on Arbitrary Smooth Surfaces," Ph.D. dissertation, The Ohio State University, Department of Electrical Engineering, Columbus, Ohio, Summer 1982. Also, see Volakis et al., IEEE Trans. Antennas and Prop., Vol. AP-33, No. 7, pp. 736-743, July 1985.

[24] H.H. Chung and W.D. Burnside, "General 3-D Airborne Antenna Radiation Pattern Code User's Manual," The Ohio State University ElectroScience Laboratory, Report 711679-10, Columbus, Ohio, July 1982.

[25] J.J. Kim and W.D. Burnside, "Simulation and Analysis of Antennas Radiating in a Complex Environment," IEEE Trans. on Antennas and Propagation, AP-34, No. 4, pp. 554-562, April 1986.

[26] L.B. Felsen, "Plane Wave Scattering by Small Angle Cones," IRE Trans., AP-5, pp. 121-129, January 1957.

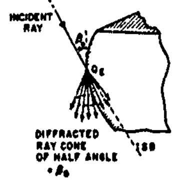

(a) diffraction by a curved wedge

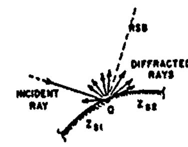

(b) diffraction at a discontinuity in surface impedance (Zs_1 and Zs_2)

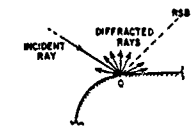

(c) diffraction at a discontinuity in surface curvature

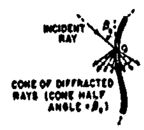

(d) diffraction by a thin curved wire

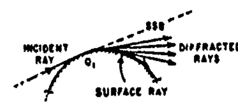

(e) diffraction by a smooth convex surface

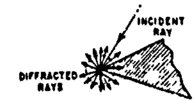

(f) diffraction by a vertex in a plane screen

Figure 1. Examples of diffracted rays

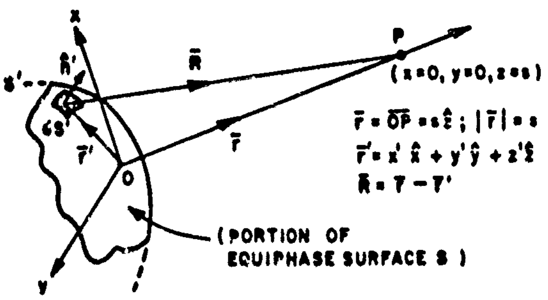

Figure 2. Equiphase (or wavefront) surface

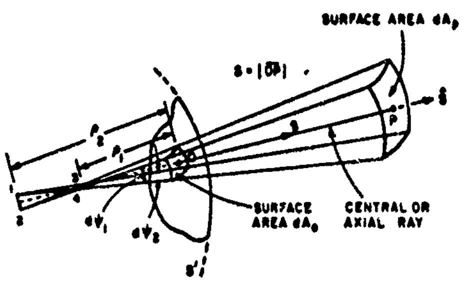

Figure 3. Ray tube geometry associated with the ray path $\overline{OP}$

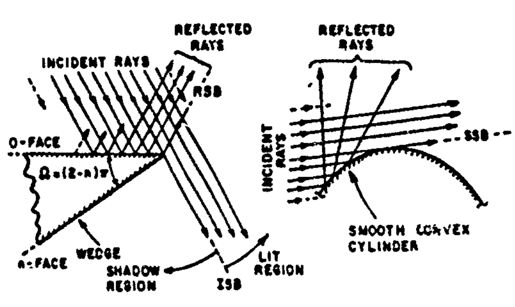

Figure 4. Examples of shadow and reflection boundaries

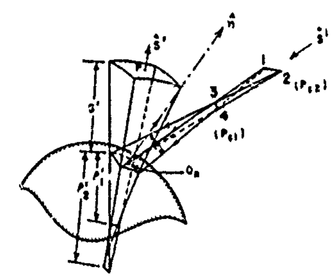

Figure 5. Reflected wavefront geometry

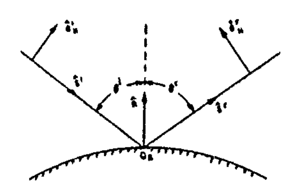

Figure 6. Unit vectors fixed in the incident and reflected rays

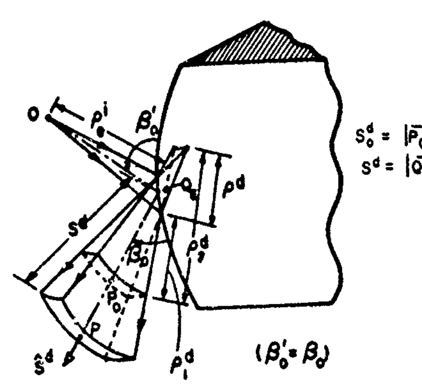

Figure 7. Edge diffracted ray tube

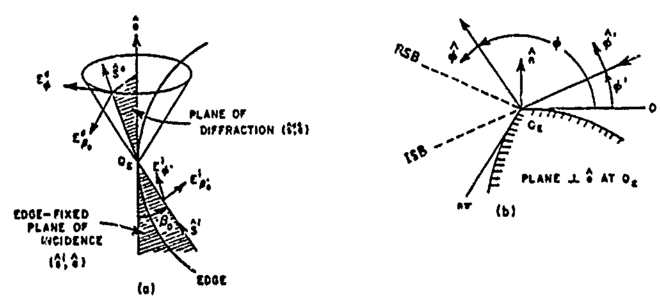

Figure 8. Edge fixed planes of incidence and diffraction

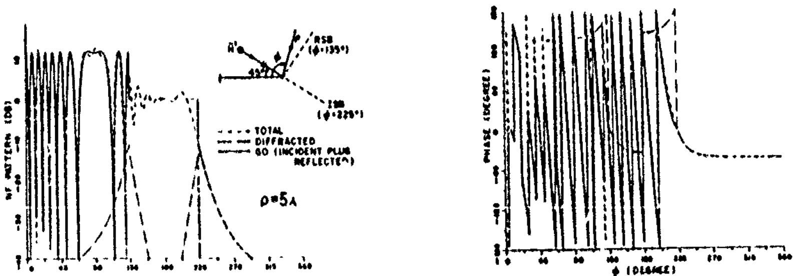

(a) magnitude

(b) phase

Figure 9. Continuity of the total UTD field surrounding a perfectly-conducting half plane excited by a plane wave

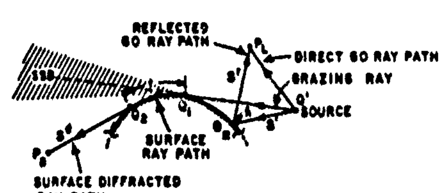

Figure 10. Diffraction at a convex surface

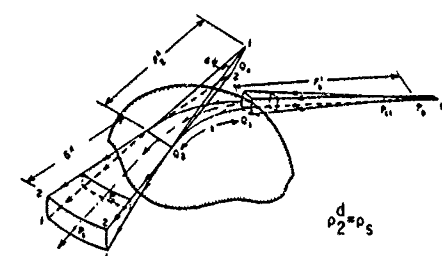

Figure 11. Surface diffracted ray path

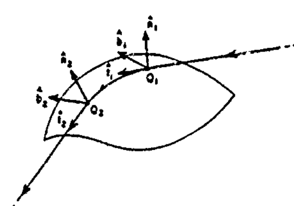

Figure 12. Unit vectors fixed in the surface ray

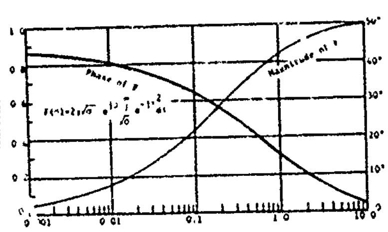

Figure 13. Plot of F(σ) versus σ

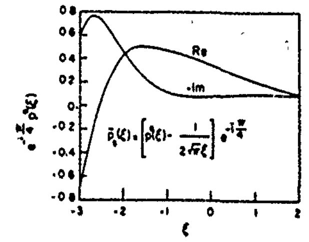

Figure 14. Plot of $e^{-j\pi/4}p^*(\xi)$ versus ξ

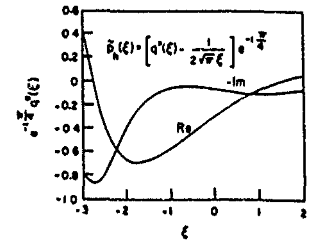

Figure 15. Plot of $e^{-j\pi/4}q^*(\xi)$ versus ξ

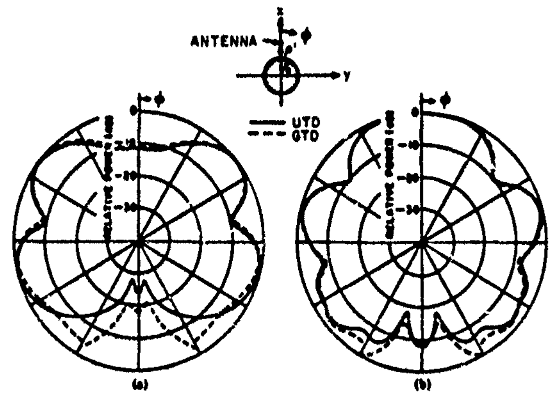

Figure 16. Comparison between GTD and UTD solutions for the radiation by electric (a) and magnetic (b) line sources in the presence of a circular cylinder. Here $a=1\lambda$ and $\rho'=2\lambda$.

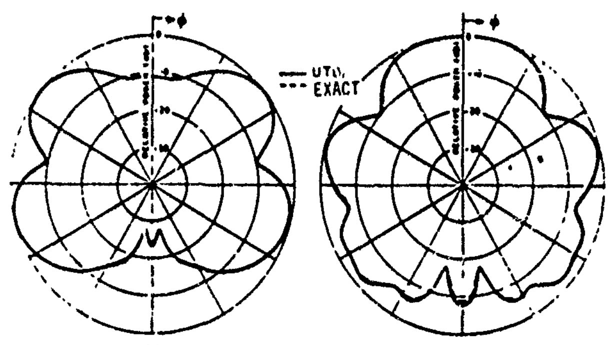

Figure 17. Comparison of UTD solutions of Fig. 16 with exact (eigenfunction) solutions

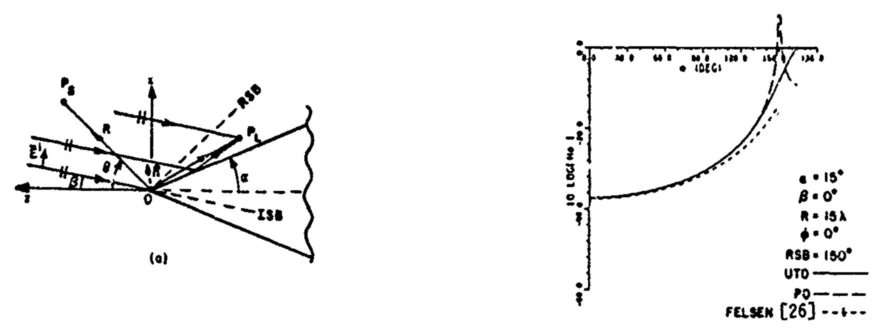

Figure 18. Magnetic field H_ϕ scattered by a semi-infinite, perfectly-conducting right circular cone when illuminated with a plane wave E_θ^i

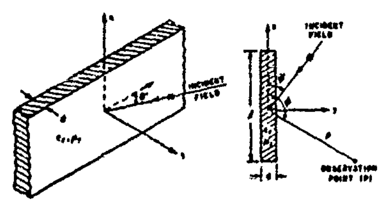

Figure 19. Plane wave incident on a dielectric/ ferrite strip

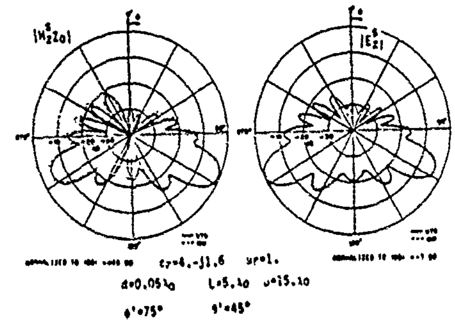

Figure 20. Magnitude of the scattered E_z^s and H_z^s fields for a E_θ^i-polarized incident plane wave

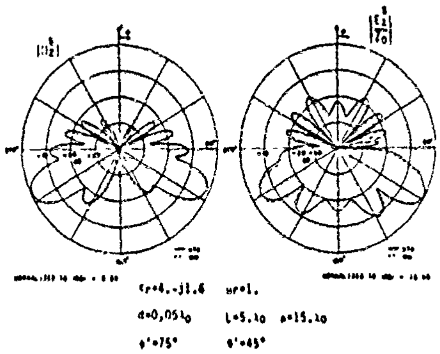

Figure 21. Magnitude of the scattered E_z^s and H_z^s fields for a H_θ^i (or E_ϕ^i)-polarized incident plane wave

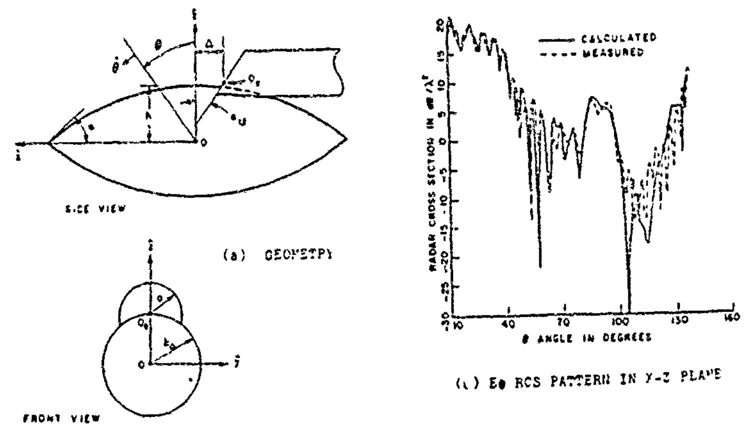

Figure 22. Radar cross section of an ogive with a circular duct

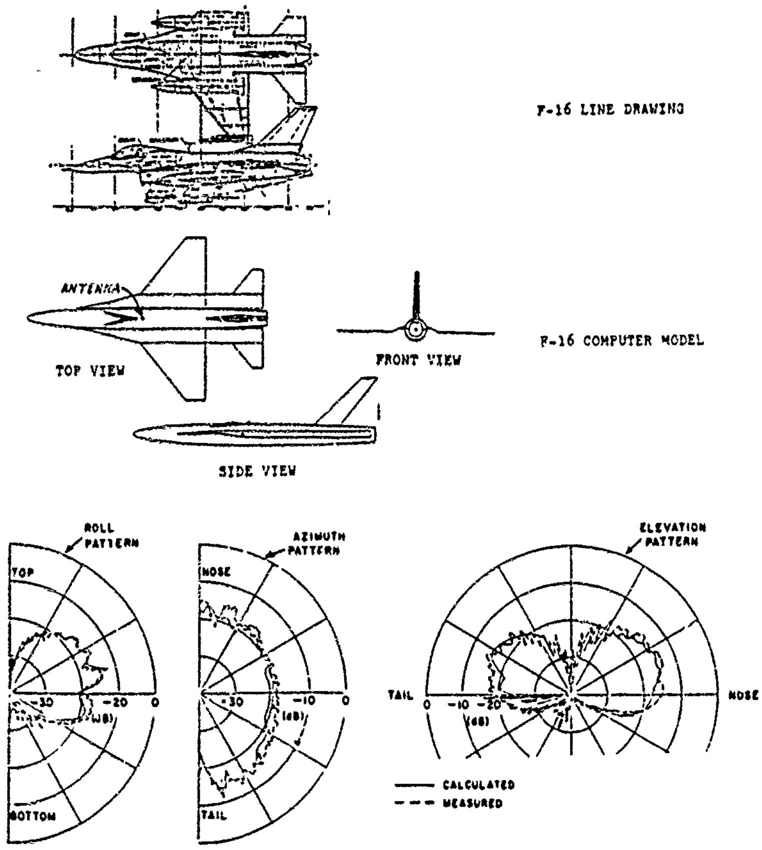

Figure 23. Radiation patterns of a monopole on an F-16 aircraft